Materials Today Bio 26 (2024) 101080

Contents lists available at ScienceDirect

Materials Today Bio

journal homepage: www.journals.elsevier.com/materials-today-bio

Enhanced hyaline cartilage formation and continuous osteochondral regeneration via 3D-Printed heterogeneous hydrogel with multi-crosslinking inks

Zhonglian Wu [a], Hang Yao [a,**], Haidi Sun [a], Zehao Gu [a], Xu Hu [b], Jian Yang [c], Junli Shi [a], Haojun Yang [d], Jihang Dai [e], Hui Chong [a], Dong-An Wang [b], Liwei Lin [f,g,***], Wang Zhang [a,g,*]

[a] School of Chemistry and Chemical Engineering, Yangzhou University, Yangzhou, Jiangsu, 225009, PR China
[b] Department of Biomedical Engineering, City University of Hong Kong, Kowloon Tong, Hong Kong SAR, 999077, PR China
[c] Clinical Medical College, Yangzhou University, Yangzhou, Jiangsu, 225001, PR China
[d] The Affiliated Changzhou, No. 2 People's Hospital of Nanjing Medical University, Changzhou, Jiangsu, 213004, PR China
[e] Department of Orthopedics and Sports Medicine, Northern Jiangsu People's Hospital, Yangzhou, Jiangsu, 225001, PR China
[f] School of Petrochemical Engineering, Changzhou University, Changzhou, Jiangsu, 213164, PR China
[g] Department of Applied Bioengineering, Graduate School of Convergence Science and Technology, Seoul National University, Seoul, 08826, Republic of Korea

ARTICLE INFO

Keywords:
Bionic hydrogel
3D printing
Gradient crosslinking
osteochondral repair
Hyaline cartilage

ABSTRACT

The unique gradient structure and complex composition of osteochondral tissue pose significant challenges in defect regeneration. Restoration of tissue heterogeneity while maintaining hyaline cartilage components has been a difficulty of an osteochondral tissue graft. A novel class of multi-crosslinked polysaccharide-based three-dimensional (3D) printing inks, including decellularized natural cartilage (dNC) and nano-hydroxyapatite, was designed to create a gradient scaffold with a robust interface-binding force. Herein, we report combining a dual-nozzle cross-printing technology and a gradient crosslinking method to create the scaffolds, demonstrating stable mechanical properties and heterogeneous bilayer structures. Biofunctional assessments revealed the remarkable regenerative effects of the scaffold, manifesting three orders of magnitude of mRNA upregulation during chondrogenesis and the formation of pure hyaline cartilage. Transcriptomics of the regeneration site *in vivo* and scaffold cell interaction tests *in vitro* showed that printed porous multilayer scaffolds could form the correct tissue structure for cell migration. More importantly, polysaccharides with dNC provided a hydrophilic microenvironment. The microenvironment is crucial in osteochondral regeneration because it could guide the regenerated cartilage to ensure the hyaline phenotype.

1. Introduction

The repair of osteochondral injuries has long posed a significant and complex challenge in treating osteoarthritis. The combination of mechanical damage, traumatic aging events, and inflammatory responses makes it difficult to achieve the desired regeneration in clinical practice [1]. Currently, research on osteochondral repair mainly focuses on tissue-engineering methods. However, the restoration of the heterogeneity while maintaining a continuous gradient interface during osteochondral regeneration remains challenging [2]. Its primary concern is forming a cartilage layer with a functional hyaline phenotype under avascular and nonneural conditions [3]. Second, the frequently overlooked aspect of rebuilding the calcification layer leads to tissue disjunction between the regenerated cartilage and subchondral bone, posing a significant obstacle to overall regenerative capacity [4,5]. Third, replicating the intricate gradient structure of natural osteochondral tissue using conventional fabrication techniques is challenging [6]. Therefore, attention and resolution of these disadvantages are essential for osteochondral regeneration.

The matrix components inherent in the hyaline cartilage at the joint site serve as the biochemical foundation for the intricate functions of the bone joint. Extensive research has demonstrated the ability of the

* Corresponding author. School of Chemistry and Chemical Engineering Yangzhou University Yangzhou, 225009, PR China.
** Corresponding author.
*** Corresponding author. School of Petrochemical Engineering Changzhou University, Changzhou, 213164, PR China.
E-mail addresses: yaohang@yzu.edu.cn (H. Yao), lin-official@snu.ac.kr (L. Lin), zhangwang@yzu.edu.cn, zhangwang@snu.ac.kr (W. Zhang).

https://doi.org/10.1016/j.mtbio.2024.101080
Received 17 January 2024; Received in revised form 16 April 2024; Accepted 1 May 2024
Available online 3 May 2024
2590-0064/© 2024 The Authors. Published by Elsevier Ltd. This is an open access article under the CC BY-NC-ND license (http://creativecommons.org/licenses/by-nc-nd/4.0/).

hyaline cartilage to withstand complex compressive and shear stresses, thereby providing a stable cellular microenvironment for subchondral bone cells [7]. Researchers initially introduced stem cells and growth factor induction into the regeneration materials to accelerate hyaline cartilage formation in osteochondral repair [8]. Additionally, manipulating material activity or using paracrine effects to stimulate the migration of surrounding chondrocytes has proven to be a practical approach [9]. However, the physicochemical microenvironment provided by the material, particularly its hydrophilic and viscoelastic properties, also significantly influences the formation and maintenance of the hyaline cartilage matrix [10]. For example, hydrophilic polysaccharides have been identified as inhibitors of chondrocyte focal adhesion, thereby impeding the fibrotic phenotype and promoting the production of more collagen type II (COL II) than collagen type I (COL I) [11]. Therefore, focusing on the interaction between cartilage layer materials and chondrocytes to achieve hyaline matrix formation is vital.

The calcification cartilage zone (CCZ) is a pivotal interfacial structure crucial for transmitting mechanical stress and regulating fluid exchange between the hyaline cartilage and the subchondral bone [12]. Numerous studies have focused on constructing an integrated scaffold for the CCZ interface by employing the same continuous phase and relying on gravity to bond the upper and lower layers [13]. However, the heterogeneity inherent in the osteochondral tissue has often been overlooked during the preparation of the calcification layer. Owing to the physiological distinctions between cartilage and subchondral bone, using heterogeneous materials to simulate the hyaline cartilage and subchondral bone is necessary. In a notable example, Da et al. [14] successfully achieved osteochondral regeneration by preparing a heterogeneous scaffold with robust interfacial forces using dissolving conglutination and lyophilized compression methods. Therefore, the fabrication of osteochondral structures with stable mechanical interfaces is critical.

The preparation of integrated scaffolds to replicate the bionic structure has consistently captured the attention of researchers. Nevertheless, the distinct components and structural characteristics of the cartilage layer and subchondral bone limit the use of traditional preparation methods [15]. Some researchers have successfully utilized three-dimensional (3D) printing to create integrated gradient scaffolds for osteochondral tissues, thereby presenting a promising avenue for guiding tissue regeneration [16,17]. Currently, the most effective method involves using purified natural proteins or polysaccharide hydrogels, such as collagen, sodium alginate, and hyaluronic acid, with the active stimulus of the target tissue for layer-by-layer printing molding [18]. Despite these advancements, comprehensive research that details the ink-flow dynamics from pre-extrusion within the nozzles to post-extrusion solidification on the platform is still lacking, which is crucial for understanding structural stability, guiding cell migration, and matrix secretion. Therefore, a combination of multiple crosslinking methods is required to construct an ideal 3D-printed osteochondral-integrated heterogeneous scaffold.

Based on the current research status and critical challenges in osteochondral repair, precise fabrication of structures within the cartilage layer and subchondral bone is pivotal. This endeavor aimed to authentically achieve hyaline cartilage formation and establish a mechanical framework for the calcification layer. This study's initial focus was to develop inks suitable for bioprinting. The first type comprised a

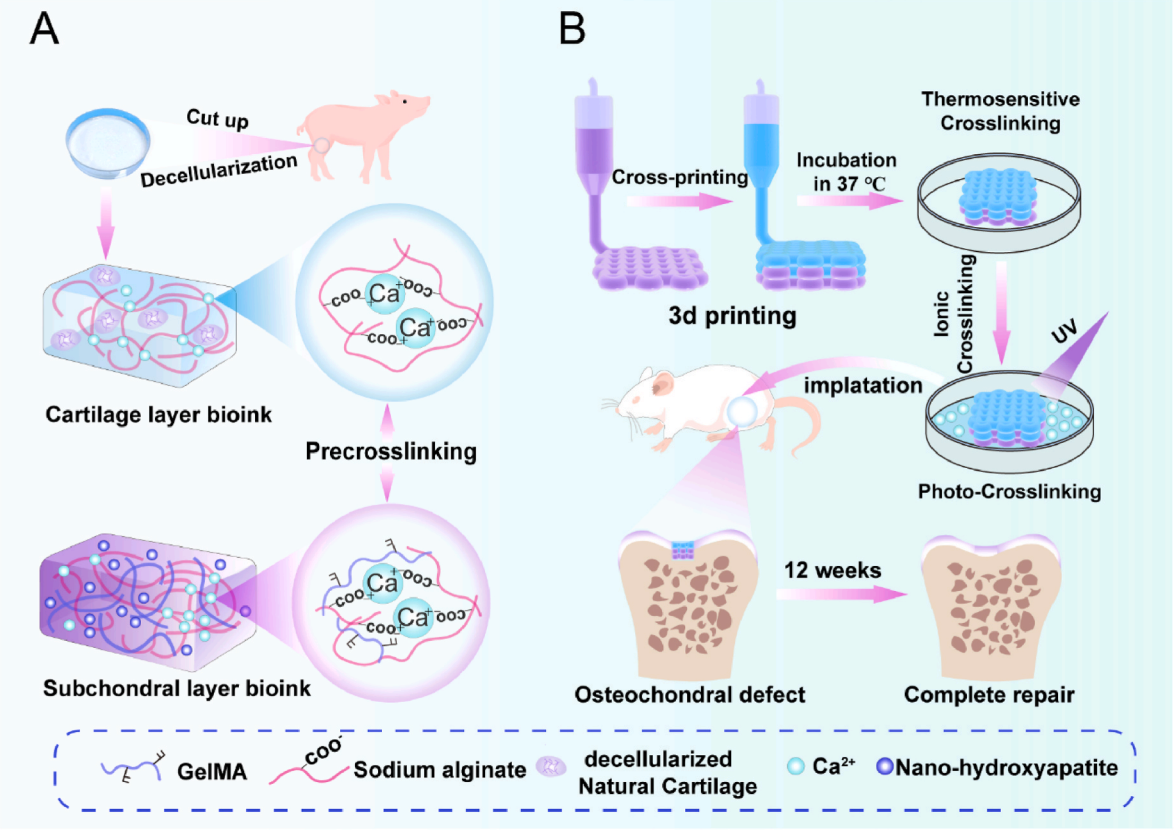

Fig. 1. Schematic of bioink formulation and 3D bioprinting to create heterogeneous constructs to repair osteochondral defects. A) Cartilage layer bioink (blue) was formed by sodium alginate with certain Ca^{2+} and decellularized natural cartilage (dNC). The subchondral layer bioink (purple) was formed by sodium alginate with a certain amount of Ca^{2+}, gelatin methacryloyl (GelMA), and nano-hydroxyapatite (nHA). B) Illustration of 3D printing biphasic constructs for osteochondral defect repair. Multiple crosslinking methods were employed in combination. This entailed initial low-concentration calcium ion pre-crosslinking, thermosensitive crosslinking, high-concentration Ca^{2+} second crosslinking, and finally, photocrosslinking. The transitional zone was constructed using a dual-nozzle cross-printing approach. The biphasic scaffold was transplanted into the osteochondral defect area of a rat for osteochondral regeneration.

pre-crosslinked upper-layer printing ink (depicted in blue) incorporating sodium alginate (SA), decellularized natural cartilage (dNC), and a small amount of $CaCl_2$. The second type was a pre-crosslinked lower-layer printing ink (depicted in purple) comprising SA, gelatin methacryloyl (GelMA), nano-hydroxyapatite (nHA), and a small amount of $CaCl_2$ (Fig. 1A). The inks exhibited excellent printing rheology and specific biological activity through optimized proportioning. Subsequently, a dual-nozzle cross-printing technology and the gradient crosslinking method were applied to construct refined osteochondral structures, particularly the calcification layers (Fig. 1B). Finally, the ensuing stages involved conducting animal experiments and exploring cell–scaffold interactions through *in vitro* testing. Further studies are required to elucidate the relationship between the complex polysaccharide ink and refined microstructure construction, which is crucial for hyaline chondrogenic and osteochondral structure regeneration.

2. Materials and methods

2.1. Materials

SA (15–25 cP, 1 % in H_2O), Triton X-100, 2-hydroxy-4-(2-hydroxyethoxy)-2-methylpropiophenone (I2959), dithiothreitol (DTT), papain, and gelatin were purchased from Sigma-Aldrich (USA). Methacrylic anhydride (MA), calcium chloride ($CaCl_2$), deuterium oxide (D_2O), sodium hydroxide (NaOH), ethylenediaminetetraacetic acid (EDTA), and HA nanopowder (nHA) were purchased from Aladdin (China). Trypsin–EDTA solution, phosphate-buffered saline (PBS), penicillin–streptomycin (PS), cell counting kit-8 (CCK-8), Calcein/PI Cell Viability/Cytotoxicity Assay Kit, and Actin-Tracker were procured from Beyotime Biotechnology (China). Dulbecco's modified Eagle's medium (DMEM) with high or low glucose was purchased from Gibco (Thermo Fisher Scientific, USA), and fetal bovine serum (FBS) was purchased from Corning (USA).

2.2. Preparation method

2.2.1. Preparation of GelMA and dNC

GelMA was synthesized by dissolving 5 g of gelatin in 50 mL of PBS at 50 °C, followed by the dropwise addition of 4 mL of MA. The reaction was allowed to proceed for 2 h. After that, the reaction solution was poured into a dialysis bag with a molecular weight cut-off of 8000–14000 DA. This solution was dialyzed for 5 d and freeze-dried to obtain GelMA.

Fresh pig cartilage was cut and crushed using a blender to prepare the NC fragments. The resulting fragments were then subjected to a decellularization treatment involving sequential exposure to surfactant Triton X-100 for 48 h at 37 °C, NaOH for 45 min at 2–8 °C, and DNAse for 3 h at 37 °C. This treatment resulted in the formation of dNC fragments.

2.2.2. Preparation of printing inks

Preparation of the upper-layer inks: A 5 % w/v SA solution was mixed with 0.01, 0.02, and 0.04 mol/L $CaCl_2$ solution. Meanwhile, 15 % w/v dNC (<150 μm) and 5 % w/v SA solutions were mixed with 0.01, 0.02, and 0.04 mol/L $CaCl_2$ solution separately. The prepared solutions were placed in a refrigerator at 4 °C overnight for degassing.

Preparation of lower-layer inks: 0.02 mol/L $CaCl_2$, 0.5 % w/v I2959, and 5 % w/v SA were added to a 10 % w/v GelMA solution to obtain Gel-SA solution. Subsequently, 2 % (w/v) nHA was added to the Gel-SA solution to obtain the Gel@nHA-SA solution.

2.3. Characterization of printing inks

2.3.1. Characterization of components of printing inks

Freeze-dried dNC samples were digested overnight in a 0.3 mg/mL papain buffer, 0.2×10^{-9} mol/L DTT, and 0.1×10^{-9} mol/L EDTA. The DNA content of the samples was measured using the fluorescence Hoechst 33258 assay [19]. Glycosaminoglycan GAG content was determined using the 1,9-dimethyl-methyl blue dye-binding method [20], whereas total collagen content was determined using the hydroxyproline method [21].

The degree of GelMA substitution was determined using a proton nuclear magnetic resonance (^{1}H NMR) spectrometer (400 MHz, Agilent, USA). The nHA content was determined using X-ray diffractometry (XRD; D8 Advance, Bruker, Germany). Fourier-transform infrared spectroscopy (FT-IR; Thermo Fisher Scientific, USA) was used to analyze the components of the printing inks.

2.3.2. Rheological properties of printing inks

A rotary rheometer (MARS 60, Thermo Fisher Scientific, USA) was used to examine the rheological properties of the printing inks. The rheological test temperature of the upper-layer ink was room temperature (25 °C), whereas all rheological tests performed on the lower-layer inks were conducted at 37 °C, except for the temperature-sweep test. The viscosity of the inks was measured by gradually increasing the shear rate from 0.1 to 100 s^{-1}. Subsequently, the samples were subjected to a stress-sweep test within a stress range of 1–1000 Pa at a frequency of 1 Hz. The storage modulus (G′) and loss modulus (G″) were analyzed over a frequency range of 0.1–100 rad/s. Under ultraviolet (UV) irradiation, the G′ and G″ were measured within 5 min.

2.4. Preparation and characterization of 3D printing hydrogel scaffolds

A 3D printer (Allevi3, USA) printed hydrogel scaffolds. The bilayer scaffolds were designed using online printing software (Allevi, USA). The 3D models were hierarchically sliced and translated into G-code instructions using Repetier-Host software. Dual-nozzle printing paths were generated by writing appropriate G-code commands. The detailed setup of the 3D printing is presented in Table S1.

The hydrogel scaffolds were viewed using scanning electron microscopy (SEM; Gemini SEM 300, ZEISS, Germany). Wet-gradient bilayer hydrogel scaffolds were subjected to frozen sectioning using a freezing microtome (CM1950, Leica, Germany).

2.5. Mechanical properties of bilayer hydrogel scaffolds

The compressive modulus of the scaffold was evaluated using a universal testing machine (WDW-10, Shanghai Hualong, China), and the resistance of the scaffold to oscillations was assessed using a rheometer (MARS 60, Thermo Fisher Scientific, USA). The testing was conducted at a constant oscillation amplitude (γ) of 1 % and oscillation frequencies ranging from 0.1 to 10 Hz.

2.6. Swelling and degradation properties of the bilayer scaffolds

The initial dry weights of the samples (W_0) were recorded before immersion in deionized water. After a specified period, excess water in the samples was carefully wiped off using Kimwipes, and the weight was measured (W_t). The swelling ratio was calculated using the following equation:

$$\text{Swelling ratio}\ (\%) = ((W_t - W_0) / W_0) \times 100\%$$

For the degradation test, freeze-dried scaffolds were immersed in a simulated body fluid and placed in a shaker. At 1, 3, 7, 14, 21, and 28 d, freeze-dried samples were collected and weighed (W_d), and the degradation rate was calculated using the following equation:

$$\text{Degradation rate}\ (\%) = ((W_0 - W_d) / W_0) \times 100\%$$

2.7. In vitro cytocompatibility studies

2.7.1. Cell cytotoxicity assay and morphology assessment

The scaffolds were soaked in DMEM supplemented with 10 % FBS and 1 % PS for 24 h. The chondrocytes and BMSCs were seeded in a 24-well plate at a density of 2×10^4 cells/well. The cells were cultured in DMEM soaked in the scaffolds. At 1, 4, and 7 d, CCK-8 and live/dead stain assay kits were used to detect cell proliferation.

2.7.2. Cell attachment assay

The upper or lower scaffolds (diameter = 6 mm, height = 1 mm) were placed in the upper chamber of a transwell in the 24-well plate. Then, the cells were seeded on the upper or lower scaffolds at a density of 2×10^5 cells/well. After 7 d, the cell scaffolds were stained with a phalloidin solution for 1 h to visualize the actin filaments. Finally, confocal laser scanning microscopy (LSM 880, ZEISS, Germany) was used to observe the adhesion behavior of the cells.

2.7.3. Chondrogenesis and osteogenesis evaluation mRNA expression analysis of chondrogenesis and osteogenesis in vitro

The upper or lower scaffolds (diameter = 6 mm, height = 1 mm) were placed in the upper chamber of a transwell in the 24-well plate. Subsequently, a suspension of chondrocytes at a density of 2×10^5 cells/scaffold or well was dropped onto the upper layer scaffolds (SA and SA@dNC groups) and in 6-well plates (two-dimensional (2D) culture chondrocytes as the control group) to evaluate the chondrogenic effect. To assess osteogenic ability, BMSCs were seeded on the lower layer of the Gel–SA (control group) and Gel@nHA-SA scaffolds. After 21 d, the samples were collected for immunofluorescence (IF) staining and qRT-PCR. IF staining was performed according to the manufacturer's protocol (Abcam). The RNA was extracted using the TRIzol precipitation method. qRT-PCR was performed using a MyGo Pro real-time PCR detection system (IT-IS, UK) to quantify gene expression levels. The primers used for each gene are listed in Table S2 and S3.

2.8. In vivo osteochondral repair in Sprague–Dawley rat

Experimental procedures involving animals were approved by the Laboratory Animal Welfare Ethics Committee of Yangzhou University (approval number: 202211015). Male Sprague–Dawley (SD) rats were randomly divided into four groups: G-control, G-nHA, G-dNC/nHA, and Control. An osteochondral defect (2.0 mm in diameter and 2.0 mm in height) was drilled into the femoral trochlea. The hydrogel scaffold block was then carefully implanted into the osteochondral defect.

2.9. Biomechanical testing

The knee junctions of rats were excised after 12 weeks. Mechanical testing was performed using a modified rheometer (MARS 60, Thermo Fisher Scientific, USA) with a 50-N maximum loading force sensor. A cylindrical indenter with a diameter of 1 mm was used to press the region of the newly grown tissue. The load-displacement curve was obtained by advancing the indenter at a speed of 0.01 mm/s. The unconfined Young's modulus of the cartilage was determined by calculating the slope of the elastic region of the stress-strain curve [22].

2.10. Micro-CT analysis

The samples were scanned using a micro-CT instrument (SkyScan 1176, Bruker, Germany). During scanning, a pixel size of 18 μm pixel size was maintained. A column with a diameter of 2.0 mm and a height of 2 mm was established to precisely define the region of interest (ROI). Various subchondral bone parameters, including bone mineral density (BMD) and bone volume per total volume (BV/TV), were measured within this well-defined region.

2.11. Histological analysis

The resulting tissue sections were sliced at a thickness of 5 μm using a paraffin slicing machine (HistoCore BIOCUT, Leica Germany). The sections were stained with hematoxylin and eosin (H&E), safranin O/fast green (Saf-O/FG), Masson's trichrome (M-T), picrosirius red, and immunohistochemistry of Col I and Col II.

2.12. RNA sequencing

At week 12, the osteochondral samples were collected from the control, normal, and G-dNC/nHA groups. Subsequently, RNA sequencing was performed at Shenzhen BGI Corporation. Significance analysis was performed to identify genes that were significantly upregulated and downregulated by the G-dNC/nHA hydrogel scaffold, with a stringent threshold of $p < 0.05$.

2.13. Statistical analysis

The statistical significance of all data in this study was assessed using one-way analysis of variance. Statistical analyses were conducted using Prism software (version 8.0). Standard deviations (SDs) were used to report errors, and the level of significance was denoted as follows: $*p < 0.05$, $**p < 0.01$, $***p < 0.001$, and $****p < 0.0001$.

3. Results and discussion

3.1. Preparation and characterization of printing inks

The physicochemical properties of the ink composition directly impact the extrusion of printing ink and the properties of printed scaffolds [23]. GelMA was synthesized with a methacrylate-grafting percentage of approximately 65 %. The ^{1}H NMR spectra of the GelMA and gelatin illustrated in Figure S1A showed peaks at positions a and b (5.47 and 5.17 ppm), indicating a double bond. The morphology of nHA was identified and displayed a rod-like shape (Figure S1B). dNC has emerged as an optimal biomaterial for guiding hyaline cartilage regeneration, which could provide an instructive microenvironment conducive to tissue regeneration [24,25]. Biochemical analyses revealed remarkable differences in DNA residues and polysaccharide loss between dNC and NC (Figure S2A-C). However, overall collagen content remained relatively stable. Preservation of the collagen structure and COL II phenotype in dNC samples of various sizes was confirmed by M-T staining and IF characterization (Figure S3). Consequently, the SA polysaccharide was selected as the continuous-phase material for the printing ink to compensate for the polysaccharide lost during decellularization. dNC with a size of <150 μm and SA were chosen to simulate the upper cartilage layer, while GelMA, SA, and nHA were selected to simulate the subchondral bone layer. A 25G injection needle was used for the printing process, which could make dNC with a size of <150 μm inject smoothly from the syringe.

Rheological characterization is the most direct and effective means of understanding the printing performance of composite inks, such as extrusion smoothness and shape fidelity [26,27]. Different amounts of $CaCl_2$ were used to adjust the printability and achieve a satisfactory printing effect. As the Ca^{2+} concentration increased, the viscosity of the SA and SA@dNC inks continuously increased (Figure S4 A(i) and **B(i))**. Calcium alginate (CA) inks with increasing crosslinking degrees had a more pronounced shear-thinning behavior compared to SA (Fig. 2A). The incorporation of dNC into SA was particularly noteworthy; the ink exhibited shear-thinning behavior without Ca^{2+} (Fig. 2C). This phenomenon primarily arises from the dNC within the SA continuous phase, disrupting molecular entanglement and increasing internal friction. In summary, the SA and SA@dNC inks demonstrated shear-thinning behavior, facilitating a smooth ink flow during printing. Moreover, the modulus of the ink significantly affects the stability of printing lines

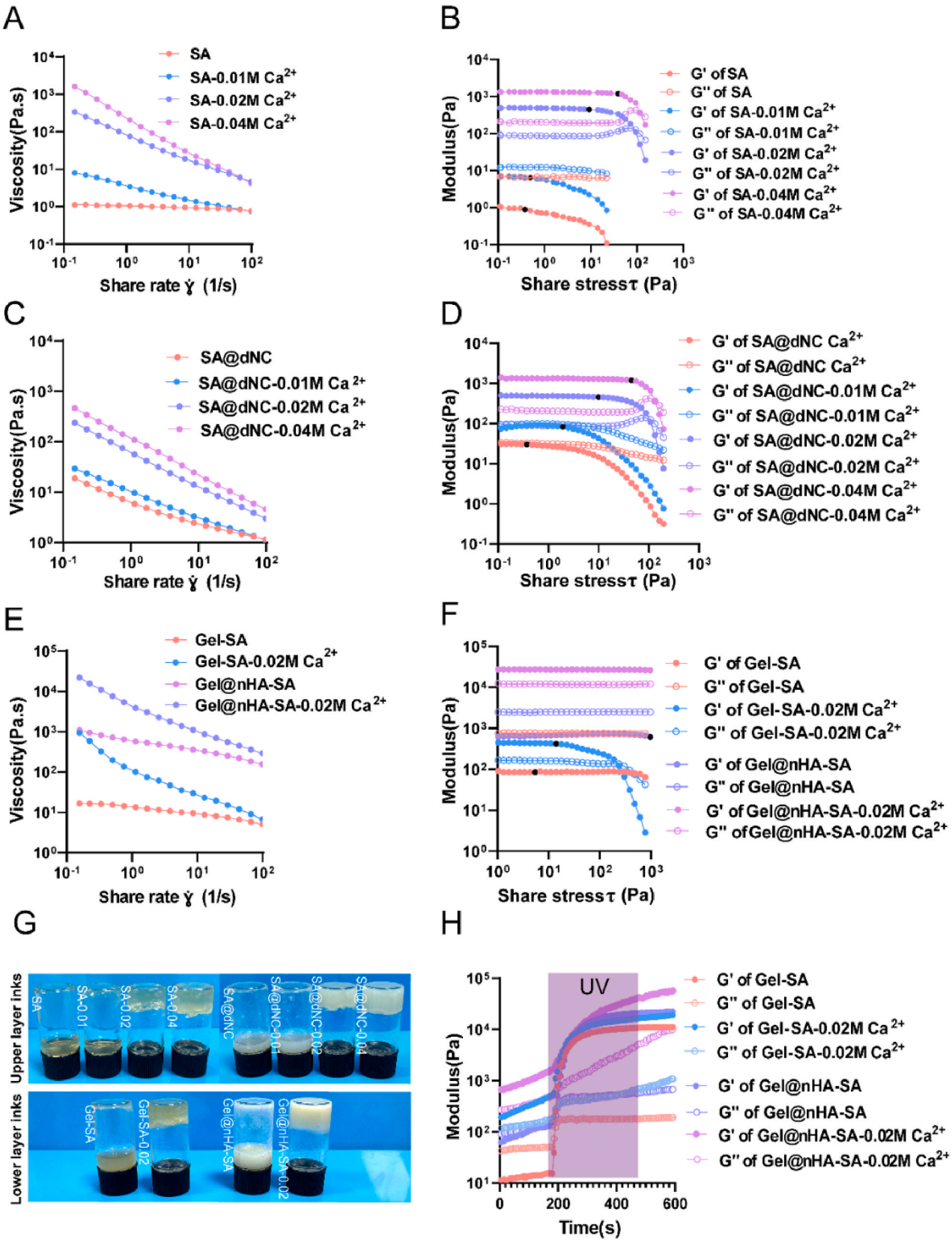

Fig. 2. Rheological properties of printing inks. A, C) Viscosity changes in SA and SA@dNC (upper-layer inks) with different pre-crosslinking degrees at 25 °C. B, D) Storage modulus (G′) and loss modulus (G″) changes in SA and SA@dNC with different pre-crosslinking degrees depending on the shear stress; the black dots represent the yield stress value. E) Viscosity changes in Gel–SA and Gel@nHA–SA (lower-layer inks) with different pre-crosslinking degrees at 37 °C. F) G′ and G″ change in Gel–SA and Gel@nHA–SA inks (lower-layer inks) with different pre-crosslinking degrees; black dot represents the yield value. G) Macrophotograph of the upper- and lower-layer inks. H) Dynamic modulus change in Gel–SA and Gel@nHA–SA inks after 5-min UV irradiation.

[28]. The modulus of the SA and SA@dNC inks increased with increasing Ca^{2+} concentrations (Figure S5A and B**)**. Oscillatory shear rheology was conducted at a frequency of 1 Hz to determine the linear viscoelastic region to ascertain a suitable degree of crosslinking of the CA inks for printing (Fig. 2B–D). As the Ca^{2+} concentration increased, the modulus of the SA and SA@dNC inks increased continuously (Figure S4 A(ii) and **B(ii))**. The yield stress, which indicates the onset of a decrease in the shear elastic modulus, was determined [29]. The yield stress of the ink increased consistently with increasing Ca^{2+} concentration. Excessive Ca^{2+} concentration resulted in over-gelation, impeding smooth ink extrusion, whereas insufficient Ca^{2+} concentration led to suboptimal mechanical performance and structural collapse. A comprehensive analysis determined that 0.02 M $CaCl_2$ was the best concentration for pre-crosslinking.

The lower-layer scaffold bears the weight of the upper layer and requires higher mechanical strength. Hence, the lower-layer ink was formulated with GelMA, SA, nHA, and 0.02 M Ca^{2+}. The addition of nHA and 0.02 M Ca^{2+} increased the viscosity of the ink (Figure S4C(i)), resulting in a relatively pronounced shear-thinning behavior (Fig. 2E). The frequency-sweep results indicated that the ink without Ca^{2+} exhibited storage modulus (G′) < loss modulus (G″), whereas the ink with Ca^{2+} exhibited G' > G'' (Figure S6A). Temperature-sweep tests revealed that the changes in the modulus were primarily driven by GelMA in the formulation (Figure S6B). Furthermore, the modulus and yield stress values of the lower-layer inks were enhanced with the addition of nHA and 0.02 M Ca^{2+}(Fig. 2F and **S4C(ii))**, which improved the mechanical performance of the ink. The modulus of the ink gradually increased over time upon exposure to UV light (Fig. 2H). The macroscopic states of all inks are illustrated in Fig. 2G. The rheological properties of the lower-layer inks demonstrated that the ink could flow smoothly from the syringe to the platform and solidify rapidly by utilizing the thermosensitive crosslinking of the GelMA hydrogel and ion crosslinking of SA. The multiple crosslinking characteristics of the ink, where the GelMA and SA hydrogels formed an interpenetrating network, resulted in extruded fibers with high fidelity and structural stability. Thus, the optimal concentration of Ca^{2+} for pre-crosslinking in the printed ink was determined to be 0.02 M.

3.2. Design and characterization of printing monolayer scaffolds

After determining the optimal ink formulation, the 3D printer successfully extruded the filaments and printed the monolayer scaffolds (Fig. 3A). These scaffolds manifested distinct pores in the range of 300–500 μm, which greatly facilitated the transportation of nutrients, oxygen, and waste materials within the fabricated scaffolds [30]. The FT-IR spectrum revealed that the characteristic peaks at 1537 cm^{-1} were associated with C–N bonds, indicating the successful incorporation of collagen components into the SA scaffold. Additionally, intense peaks were observed around 1100 cm^{-1} for the Gel@nHA–SA and Gel–SA groups, confirming the presence of nHA (Fig. 3C). The presence of nHA in the scaffold was confirmed from the XRD patterns shown in Figure S7. The scaffold with nHA exhibited characteristic peaks consistent with those of the standard nHA reference, whereas the scaffold without nHA exhibited no distinct peaks. The swelling behavior of the monolayer scaffolds was assessed to preliminarily determine their suitability (Fig. 3B). SA, which is rich in hydroxyl and carboxyl groups, exhibited the highest swelling ratio. The swelling ratio of the Gel–SA group significantly decreased, whereas that of the Gel@nHA–SA group increased. The presence of nHA hindered polymer chain entanglement, allowing water to infiltrate the hydrogels [31].

A mismatch in the swelling ratio between the upper - and lower-layer scaffold components can lead to the printed biphasic scaffold slippage at the interface [32]. Based on the swelling results of the single-layer scaffolds, the upper SA@dNC and lower Gel@nHA–SA scaffolds exhibited the slightest difference in swelling ratio. This combination of upper and lower layers may be more conducive to the formation of a stable bilayer scaffold. A dual-nozzle cross-printing strategy was adopted in this study to obtain a bilayer hydrogel with a robust interface (calcification layer), which involved programming a 3D printer to perform cross-printing in the transitional region (calcification layer) using two separate printheads (Fig. 3D and Video S1, Supporting Information**)**. A macroscopic view of the transition region and M-T staining of the cross-section of the scaffold showed that the upper and lower layers of ink crisscrossed to form a calcified layer. Subsequently, the fibers of the GelMA scaffold merged with SA at 37 °C for 3 min. Strategies for high-concentration $CaCl_2$ crosslinking and UV-light-induced photocrosslinking were adopted to prevent delamination between the upper and lower layers.

3.3. Characterization of 3D printing bilayer scaffolds

Biomimetic bilayer scaffolds, namely, G-control, G-nHA, and G-dNC/nHA, were successfully fabricated. The G-control group contained a gradient scaffold without the active materials. G-nHA denoted a gradient scaffold with the active material nHA added to the lower layer. G-dNC/nHA represented a gradient scaffold with the active material dNC and nHA added to the upper and lower layers, respectively. Cross-sectional images of the scaffolds were obtained in both wet and dry states to assess their composition and structure. Macroscopic images revealed the close adhesion of the upper and lower layers of all three scaffolds (Fig. 3E). Safranin O staining highlighted the polysaccharide SA component in red, demonstrating the close adhesion of the upper and lower layers, with SA permeating the entire scaffold. M-T staining revealed small blue fragments (dNC) in the upper part and transition region of the G-dNC/nHA group. Alizarin red staining revealed the uniform distribution of nHA in the lower part and transition region of the scaffold. The cross-section staining of the scaffold showed that the calcified layer and gradient-integrated structure were successfully prepared. The cross-sectional structure of the scaffolds was observed using SEM (Figure S8), which showed no distinct boundaries between the upper and lower layers. In the presence of dNC and nHA, the scaffold pores decreased in size.

As an ideal osteochondral tissue graft, the provision of bioactive functionality and a certain level of mechanical support is crucial [33]. The compressive properties of the bilayer hydrogel scaffolds were evaluated, as shown in Fig. 4A and **C**. The compressive modulus of the three scaffolds were 70.55 ± 4.29, 89.12 ± 15.2, and 94.64 ± 5.27 kPa, respectively. The compressive modulus of G-dNC/nHA was significantly different from that of the control group. The stress-strain curves of G-control exhibited no rupture points within a strain of 35 %, indicating excellent toughness. However, the slopes of the linear elastic regions for the G-dNC/nHA and G-nHA groups were greater than that for the G-control group, suggesting that the incorporation of nHA and dNC enhanced the mechanical performance of the scaffold. The G′ and G″ of the bilayer scaffolds were determined by rheological tests to simulate the biomechanical environment of shear stress in articular cartilage (Fig. 4B). The G-dNC/nHA group exhibited the highest shear strength. All the scaffolds remained intact after being subjected to shear stress, demonstrating the importance of fabricating a robust interface (calcification layer). Additionally, as the scaffold is ultimately transplanted into the animal body, its swelling ratio and degradation rate must be considered. The G-nHA group (570 ± 56.4 %) showed slightly higher swelling than the G-control group (485 ± 8.33 %) (Fig. 4D). The G-dNC/nHA scaffold (373 ± 14.57 %) exhibited the lowest swelling, indicating the interaction of dNC with SA. Under ideal conditions, the degradation rate of the scaffold should match the tissue growth rate [34]. During the early stages after transplantation, the scaffold provides mechanical support without rapid degradation. The degradation rate should accelerate because new tissues require growth space in the middle to later stages. The degradation rate of the G-dNC/nHA scaffolds was initially slow, but it accelerated at 3 and 4 weeks (Fig. 4E). At 3 and 4 weeks, the degradation rate of the G-dNC/nHA scaffold was

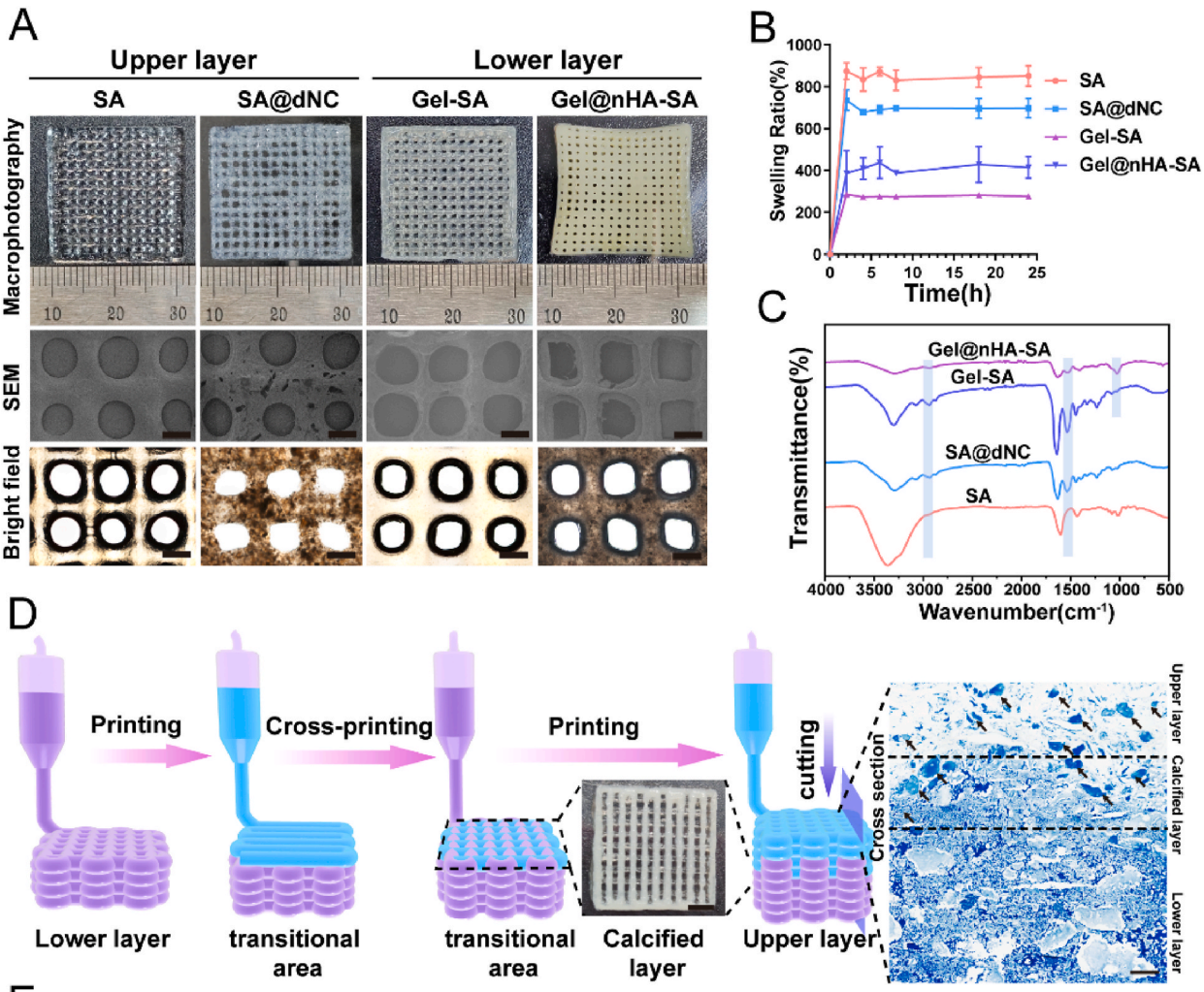

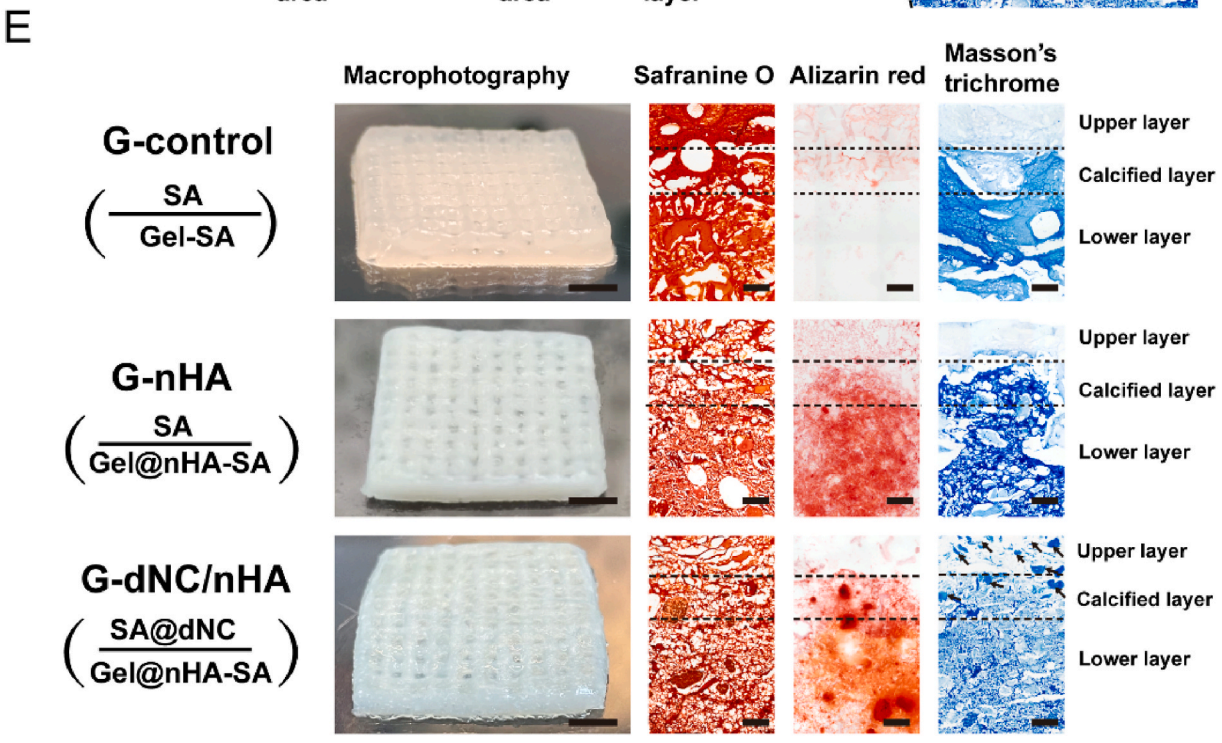

(caption on next page)

Fig. 3. Characterization of hydrogel scaffolds. A) Top view of 3D-printed monolayer hydrogel scaffolds (upper-layer inks contained SA and SA@dNC; lower-layer inks contained Gel-SA and Gel@nHA-SA) showed macrophotography, SEM, and bright-field microscopy images. Scale bar: 500 μm. B) Swelling ratios of monolayer hydrogel scaffold inks at various time intervals: 2, 4, 6, 8, 18, and 24 h. C) FT-IR spectra of hydrogel inks. D) Schematic of the 3D printing bilayer scaffold process included the top view of the calcified layer and cross-section of Masson's trichrome (M–T) staining of the scaffold. Scale bar in the top view: 2 mm. Scale bar in M-T staining image: 200 μm. E) The group naming for the bilayer scaffolds was as follows: G-control, G-nHA, and G-dNC/nHA. Components and structures of bilayer scaffolds characterized by macrophotography, safranine O staining, M-T staining, and alizarin red staining. The arrows indicate the dNC fragments. Scale bar in the macrophotograph image: 4 mm. Scale bar in the histological staining image: 200 μm

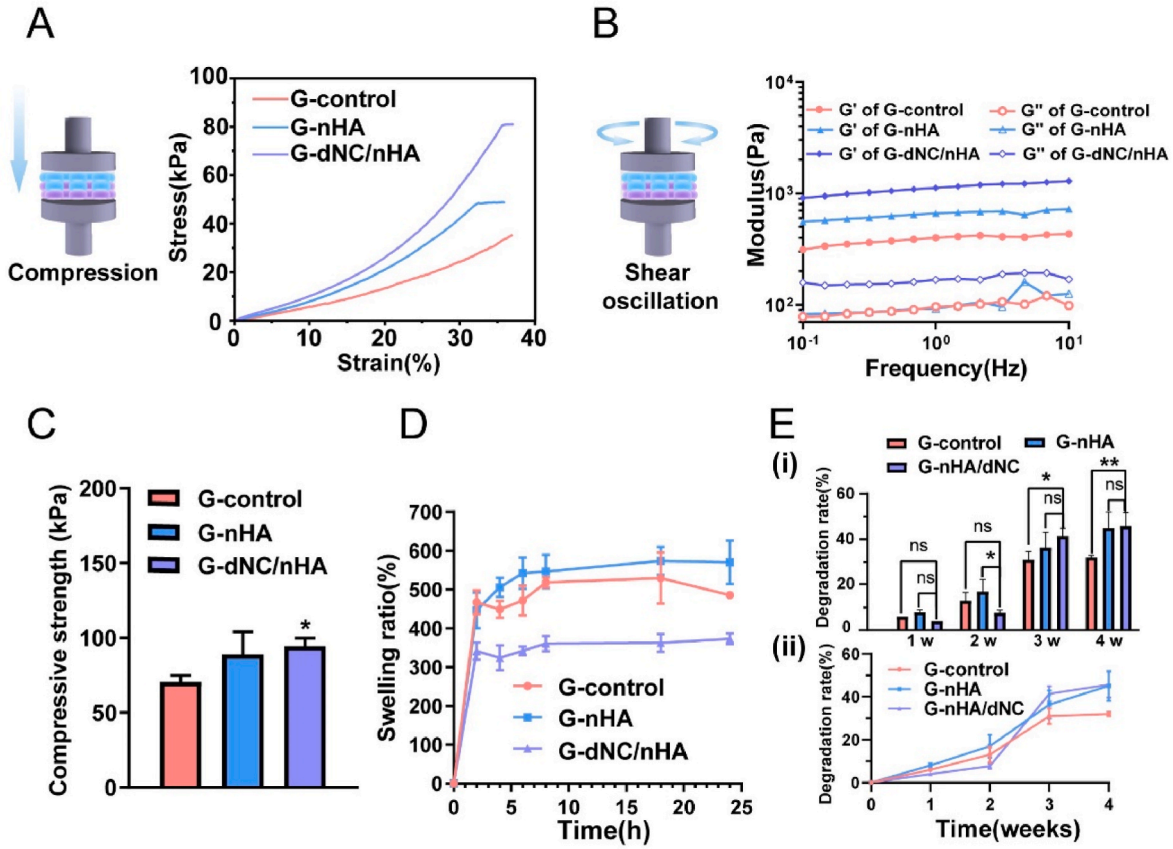

Fig. 4. Mechanical, swelling, and degradation properties of bilayer hydrogel scaffolds. A) Compressive stress-strain curves. B) G′ and G″ were determined through rheological testing under a constant oscillation amplitude (γ) of 1 % and frequency ranging from 0.1 to 10 Hz. C) Compressive strength (n = 3) at 20 % strain of bilayer hydrogel scaffolds. D) Swelling ratios and E) degradation rates of bilayer hydrogel scaffolds. The data were analyzed by one-way analysis of variance, and error bars indicate mean ± standard deviation, *p < 0.05, **p < 0.01, and ***p < 0.001.

significantly different from that of the G-control scaffold. The degradation rate of the G-dNC/nHA scaffold aligned with the requirements for an osteochondral transplant alternative.

In brief, the construction of osteochondral scaffolds should consider structural bionics, calcification layers, and hyaline cartilage phenotype [35]. First, an intricate gradient structure was created using 3D printing technology, which required the synergy of various crosslinking methods. The addition of 0.02 M Ca^{2+} before printing increased the viscosity and modulus of the extruded fiber, contributing to improved scaffold fidelity [36]. The combination of photocrosslinking and high-concentration Ca^{2+} crosslinking was beneficial for maintaining scaffold stability. Second, the stability of the osteochondral bilayer scaffold depended on the calcification layer with a robust interface force, demonstrating resistance to delamination after exposure to compression and shear forces [37]. Finally, the effects and mechanisms of dNC guiding hyaline cartilage regeneration were elucidated through *in vitro* and *in vivo* experiments.

3.4. Assessment of biocompatibility and biofunction ability of 3D-printed scaffolds in vitro

A CCK-8 assay was conducted to assess the cytotoxicity of the bilayer hydrogel scaffolds (Fig. 5A and **B)**. The cells were cultured in the untreated medium (control group). No significant difference was observed in the optical density (OD) values between each scaffold group and the control group at the same time point, indicating that the various hydrogel scaffolds did not release toxic substances affecting chondrocytes. Interestingly, the viability of the BMSCs in all scaffold groups differed significantly from that of the control group on the 7th day, indicating that the scaffolds promoted BMSCs proliferation. Live/dead staining assays were also used to assess the cell viability and morphology on days 1, 4, and 7 (Fig. 5C–S9, and **S10)**, indicating that the morphology of the cells from all groups appeared normal.

Chondrocytes and BMSCs were seeded onto the upper (cartilage layer) and lower (subchondral bone) layers to evaluate the efficacy of the designed materials in promoting osteochondral tissue repair (Fig. 5D). After 7 d, cell morphology was assessed by staining (Fig. 5E and **F)**. Chondrocytes cultured on the scaffolds exhibited an oblate morphology. SA and SA@dNC provide a hydrophilic environment that

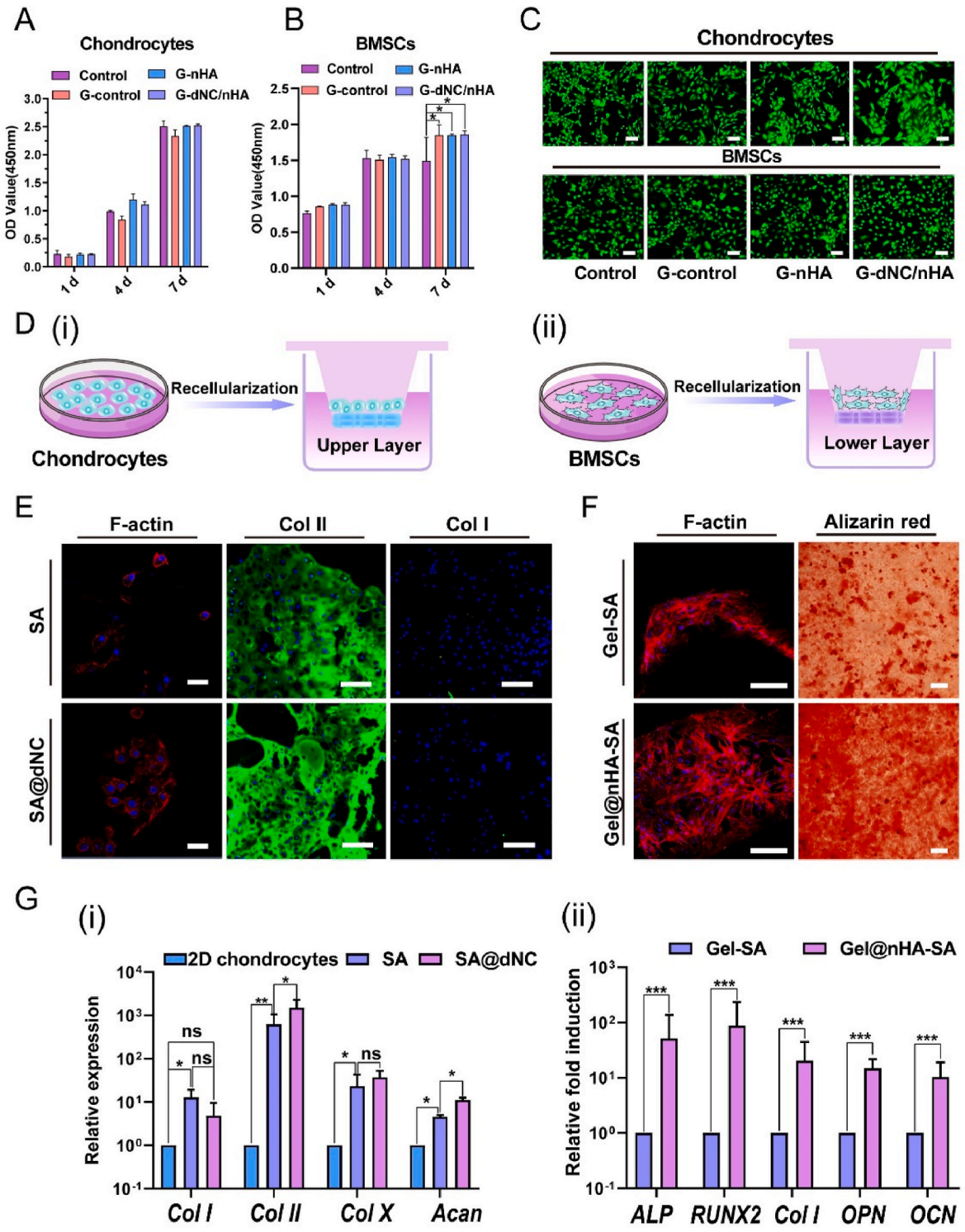

Fig. 5. Cell viability, proliferation, adhesion, chondrogenic maintenance, and osteogenic potential of the printed upper- and lower-layer hydrogels *in vitro*. A, B) Viabilities of chondrocytes and bone marrow-derived mesenchymal stem cells (BMSCs) were tested with CCK-8 (n = 3). The control group comprised cells that were cultured in an untreated medium. C) Images of live/dead staining were captured after culturing chondrocytes and BMSCs with various scaffolds for 7 d (live cells: green, dead cells: red. Scale bar: 100 μm. D) Schematic of chondrocytes and BMSCs were separately seeded on upper-layer (i) and lower-layer (ii) hydrogels. E) Image of chondrocyte adhesion morphology on scaffolds on day 7. Nucleic acids are depicted in blue, while F-actin is visualized in red. Scale bar: 40 μm. Immunofluorescence (IF) staining of collagen type II (COL II) and collagen type I (COL I) was utilized to evaluate chondrocyte phenotype. Scale bar: 200 μm. F) Images of BMSCs adhesion behavior in 7 d. Scale bar: 100 μm. Alizarin red staining was used to assess osteogenic potential. Scale bar: 400 μm. G) Chondrogenic maintenance of chondrocytes (i) and osteogenic differentiation of BMSCs (ii) were assessed at the mRNA level (qRT-PCR) (n = 3). All data were analyzed by one-way ANOVA, and error bars indicate mean ± SD, *$p < 0.05$, **$p < 0.01$, and ***$p < 0.001$.

facilitates the maintenance of normal chondrocyte morphology [38]. In addition, the dNC component preserved the collagen microstructure and reduced chondrocyte adhesion to the scaffolds. Conversely, BMSCs exhibited typical spindle- and star-shaped morphologies on the scaffolds (Gel-SA and Gel@nHA-SA). The morphology of the BMSCs was attributed to the presence of the arginine-glycine-aspartic acid (RGD) peptide sequence in GelMA, which facilitates cell attachment [39]. IF staining was conducted on the 21st day to identify the matrix secreted by the chondrocytes on the SA and SA@dNC scaffolds (Fig. 5E), which revealed a hyaline phenotype with high expression of COL II and low expression of COL I. The hydrophilic microenvironment created by SA likely contributes to maintaining the chondrocyte phenotype and preventing dedifferentiation [40]. The increased brightness of COL II in the IF of the SA@dNC group was attributed to the numerous active sites on the bioactive material dNC. As shown in Fig. 5G(i), the relative expression of COL II in the SA@dNC group differed significantly from that in the SA group. In particular, the relative expression of COL II in the SA@dNC group was compared with that in the 2D chondrocyte group, manifesting three orders of magnitude of mRNA upregulation. The relative expression of COL II in the SA@dNC group was low. The results showed that the hyaline cartilage phenotype (high expression of COL II and low expression of COL I) of the chondrocytes was maintained on the SA@dNC scaffolds. The results of the induction of BMSCs toward osteogenesis in the lower layer of the hydrogel are shown in Fig. 5F. Alizarin red staining revealed significant calcium deposition during osteogenic induction, with the Gel@nHA-SA group exhibiting a darker color than the Gel-SA group. Furthermore, the Gel@nHA-SA group showed a significantly higher expression of osteogenic-related genes than the Gel group, including ALP, RUNX2, COL I, OPN, and osteocalcin (OCN) (Fig. 5G(ii)). This indicates that GelMA and nHA stimulated

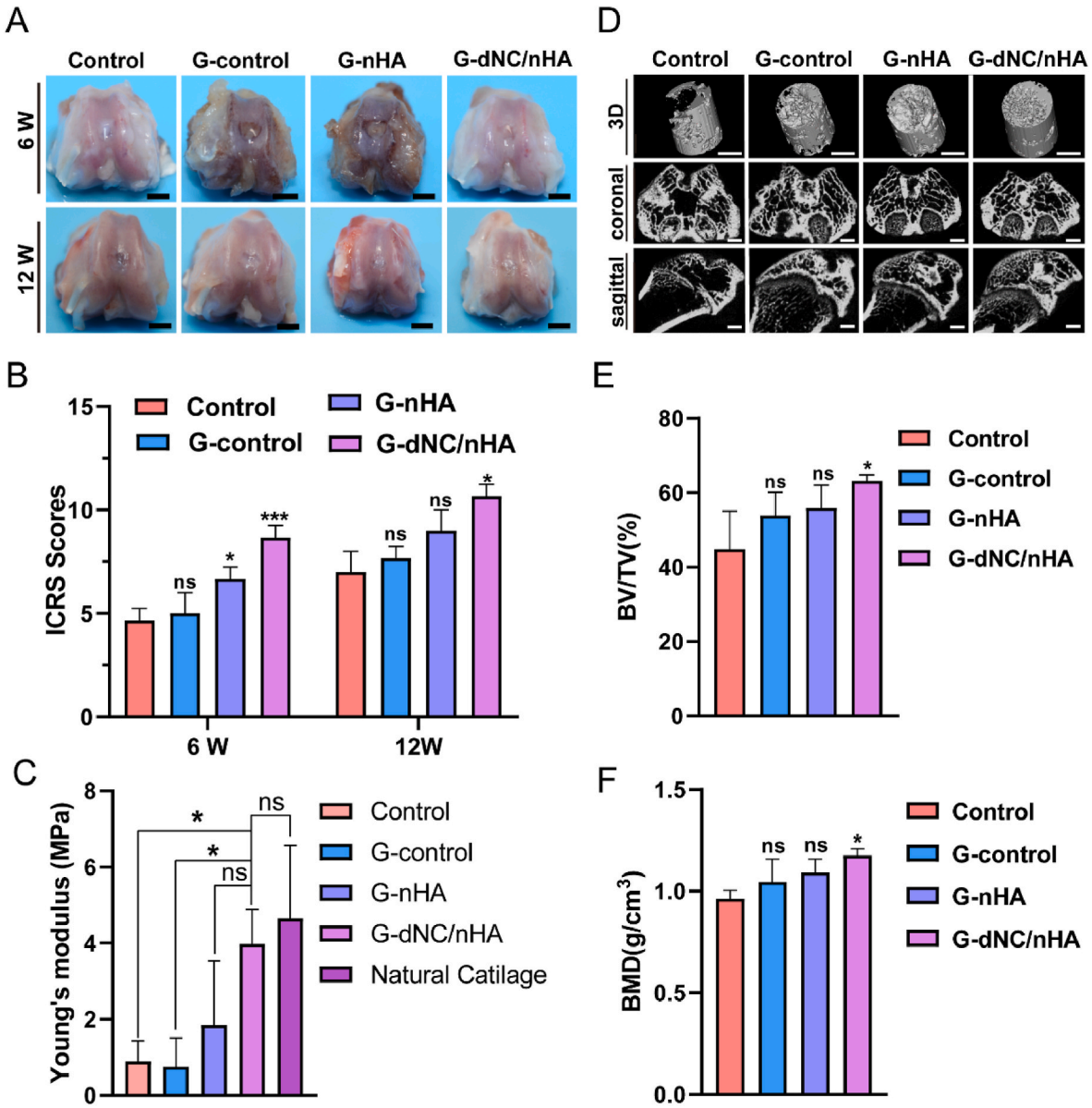

Fig. 6. Osteochondral regeneration of bilayer scaffolds implanted at rat joints *in vivo*. A) The macroscopic evaluation image of the regeneration in the femoral trochlea of rats at 6 and 12 weeks. The control group represented that the defect was not filled with a scaffold. Scale bar: 2 mm. B) Corresponding scores were based on the ICRS macroscopic scoring system (n = 6). C) Young's modulus of normal and repaired group at 12 weeks (n = 3). D) Reconstructed 3D, coronal, and sagittal images of the osteochondral defect region are displayed through micro-CT analysis at 12 weeks. Scale bar: 2 mm. E, F) Bone volume (BV), tissue volume (TV), and bone mineral density (BMD) were quantitatively evaluated based on the grayscale values extracted from the reconstructed images (n = 3). All data were analyzed by one-way ANOVA, and error bars indicate Mean ± SD, *p < 0.05, **p < 0.01, and ***p < 0.001. "ns" represents no significance.

BMSCs to undergo osteogenic differentiation.

3.5. Assessment of osteochondral regeneration in a rat model in vivo

An osteochondral defect model was established in the femoral trochlea of SD rats to evaluate repair efficacy. The bilayer hydrogel scaffolds were implanted into osteochondral defects, with the untreated group used as the control. Macroscopic photographs showed that none of the groups achieved complete regeneration in the initial 6 weeks (Fig. 6A). Newly formed fibrocartilaginous tissue in the control group exhibited a distinct milky-white appearance in the defect area, which was notably different from the surrounding normal cartilage (NC). After 12 weeks, the group treated with G-dNC/nHA demonstrated the most promising results, with the regenerated tissue closely resembling the NC. By contrast, the other groups exhibited discontinuous tissues that were not fully integrated with the surrounding tissue. Utilizing the criteria outlined by the International Cartilage Repair Society (ICRS) macroscopic scoring system (Table S4), the repair effects were evaluated and are presented in Fig. 6B. Compared to the other three groups, the G-dNC/nHA group achieved the highest scores, signifying superior repair outcomes. A compression destruction test was performed to study the biomechanical properties of regenerated tissues (Figure S11). Young's compression modulus results demonstrated that the G-dNC/nHA group (3.75 ± 1.3 MPa) exhibited mechanical properties resembling NC (4.78 ± 1.94 MPa), with a statistically significant difference from the control group (0.89 ± 0.53 MPa) (Fig. 6C). Micro-CT analysis was employed as an assessment method to evaluate the subchondral bone regeneration (Fig. 6D). Subchondral bone formation was the most pronounced in the G-dNC/nHA group, where the newly formed bone almost filled the entire subchondral region at 12 weeks. The findings indicated that G-dNC/nHA scaffold implantation significantly promoted subchondral bone growth, as evidenced by the higher BV/TV and BMD values in the all-scaffold groups than in the control group (Fig. 6E and **F**). The bone surface fraction (BS/TV), trabecular thickness (Tb. Th), trabecular number (Tb. N), and trabecular separation (Tb. Sp) values are shown in Figure S12. The newly formed bone mass was the highest in the G-dNC/nHA group, and the spatial morphology of the trabecular bone was optimal.

Histological staining assessments further validated that the G-dNC/nHA scaffold simultaneously promoted articular cartilage and subchondral bone regeneration compared to the other groups (Fig. 7). H&E staining revealed that the G-dNC/nHA group exhibited superior postoperative repair, characterized by a smooth cartilage surface, optimal remodeling between the cartilage and subchondral bone, and excellent fusion with adjacent NC. In contrast, the control group exhibited typical fibrous tissues. Although the G-control and G-nHA groups showed less favorable repair outcomes at 6 weeks postoperatively, tissue repair showed a slight improvement after 12 weeks. The extracellular matrix of cartilage primarily consists of collagen fibers and proteoglycans [41]. Saf-O/FG staining was used to illustrate proteoglycan distribution. The G-dNC/nHA group exhibited uniform proteoglycan distribution at 6 and 12 weeks. At 12 weeks, newly secreted proteoglycans were evenly distributed throughout the cartilage layer and seamlessly merged with the surrounding tissue. In addition, the staining images revealed that the G-control and G-nHA scaffolds retained undegraded components at 12 weeks postoperatively, which was consistent with the degradation data *in vitro* (Fig. 4D). In contrast, the G-dNC/nHA group exhibited the fastest degradation rate at 12 weeks, matching the growth rate of the regenerated tissue. The distribution of proteoglycans in the regenerated tissue further elucidated the regenerative mechanism, which involved new tissues growing from the edges of the defect toward the center.

M-T staining showed that the G-dNC/nHA group exhibited a consistently distributed collagen network in the regenerated cartilage layer, whereas the remaining groups displayed minor cracks on the cartilage surface. Considering the profound impact of collagen orientation and distribution on the overall characteristics of cartilage, the investigation of collagen alignment is important [42]. Picrosirius red staining revealed that the color and orientation of collagen fibers in the G-dNC/nHA group closely resembled those of NC. In contrast, the other groups exhibited collagen colors and orientations that were distinct from those of NC. Specifically, the control group displayed red-stained COL I throughout the entire osteochondral layer with a disordered orientation, indicating the presence of fibrous tissues in the regenerated tissue. Immunohistochemical (IHC) staining was performed on the collected samples to investigate the collagen phenotypes in different groups. In the control group, the regenerated cartilage region was negative for COL II expression and positive for COL I expression. Staining for COL II was much stronger in the repaired tissues of the G-dNC/nHA group than in the other three groups at both 6 and 12 weeks. The other two groups displayed collagen phenotypes with COL I and COL II expressions. The regeneration of the subchondral bone was identified by IHC staining for COL I and IF staining for OCN. The subchondral bone was positive for COL I in all groups. IHC staining revealed that the subchondral bone in each group was positive for COL I. The IF staining results for OCN showed that the positive area of G-dNC/nHA was significantly greater than that of the control group (Figure S13). The histological staining score was the highest in the G-dNC/nHA group (Figure S14 and Table S4). Moreover, the anti-inflammatory effect of the G-dNC/nHA scaffold was verified by IF staining at 6W. The results showed that the scaffold stimulated macrophages to polarize into M2 macrophages, which resisted early inflammatory response and promoted tissue repair (Figure S15).

In summary, the regenerative efficacy of the G-dNC/nHA group surpassed that of the other three groups. The suboptimal integration observed between the cartilage and the subchondral bone in the other three groups could be attributed to inadequate active stimuli and differences in the calcification layer. The hydrophilic and bioactive microenvironment created by the G-dNC/nHA scaffold proved beneficial for hyaline cartilage regeneration, which is consistent with the *in vitro* experimental results. Subchondral bone repair can be achieved through *in situ* spontaneous self-remodeling. Articular cartilage regeneration is a primary challenge in osteochondral regeneration [43]. The promotion of hyaline cartilage formation is pivotal for enhancing the integration of bone and cartilage.

The mRNA expression in the regenerated osteochondral tissues was analyzed at 12 weeks to elucidate the repair mechanisms of the scaffold. Principal component analysis (PCA) showed that the G-dNC/nHA group exhibited the mRNA expression profile like that of native osteochondral tissue (Normal group). Conversely, the G-dNC/nHA group displayed distinct mRNA expression compared to the control group (Fig. 8A). The heatmap showed the cluster of differentially expressed genes (DEGs) between the G-dNC/nHA group and the control and normal group, respectively (Fig. 8B, Figure S16). Clustering results showed differences in gene expression trends among the groups. However, there were some similar gene expression trends between the G-dNC/nHA group and the normal group. The volcano plot of G-dNC/nHA versus the control (negative control) confirmed the presence of several significantly upregulated genes in the G-dNC/nHA tissue (Fig. 8C), including Comp, Sox9, Col2a1, and Acan. However, osteogenic marker genes such as Sp7, Alpl, Spp1, and Runx2 were insignificant in the volcano plot. The volcano plot of G-dNC/nHA versus normal (positive control) confirmed that the chondrogenic and osteogenic genes of G-dNC/nHA resembled those in normal tissue (Fig. 8D). The specific chondrogenic and osteogenic gene expression levels in the G-dNC/nHA group are shown in Fig. 8E and **F**. The results of COL II expression showed that chondrogenic marker genes in the G-dNC/nHA group were upregulated compared to the control group, which were consistent with the qRT-PCR *in vitro* (Fig. 5G). This suggests that the composition and structure of the scaffold, particularly the combined action of polysaccharide SA and dNC, are crucial in the successful regeneration of hyaline cartilage [44]. However, the COL II gene expression of SA@dNC scaffold groups was quite different *in vivo* and *in vitro*. It was attributed to the different

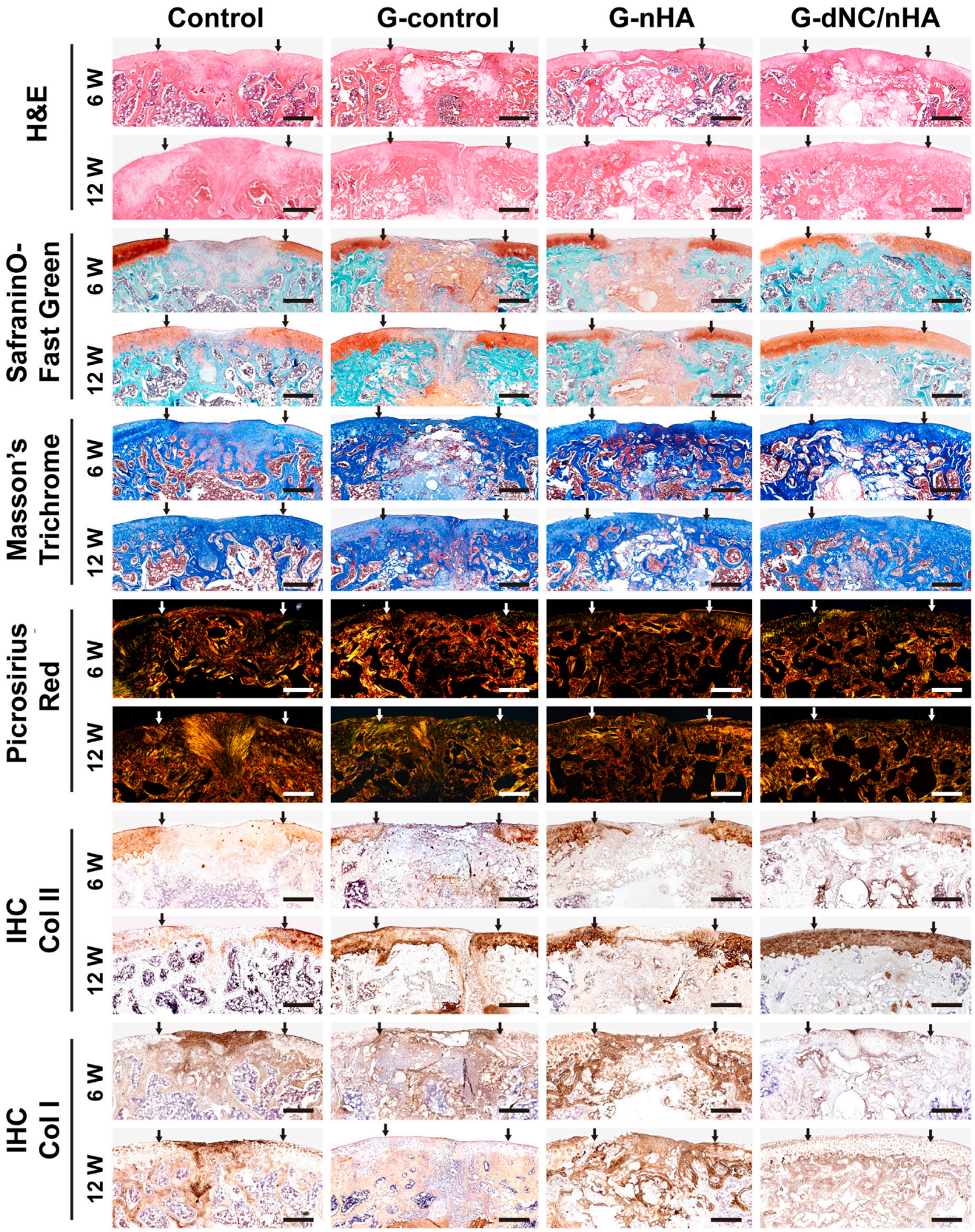

Fig. 7. Histological and immunohistochemical (IHC) staining of repaired osteochondral defects at 6 and 12 weeks *in vivo* (sagittal section), including hematoxylin and eosin, safranin O/fast green, Masson's trichrome, and picrosirius red stains. The two arrows indicate the location and width of the initially fabricated experimental defect. Scale bar: 500 μm.

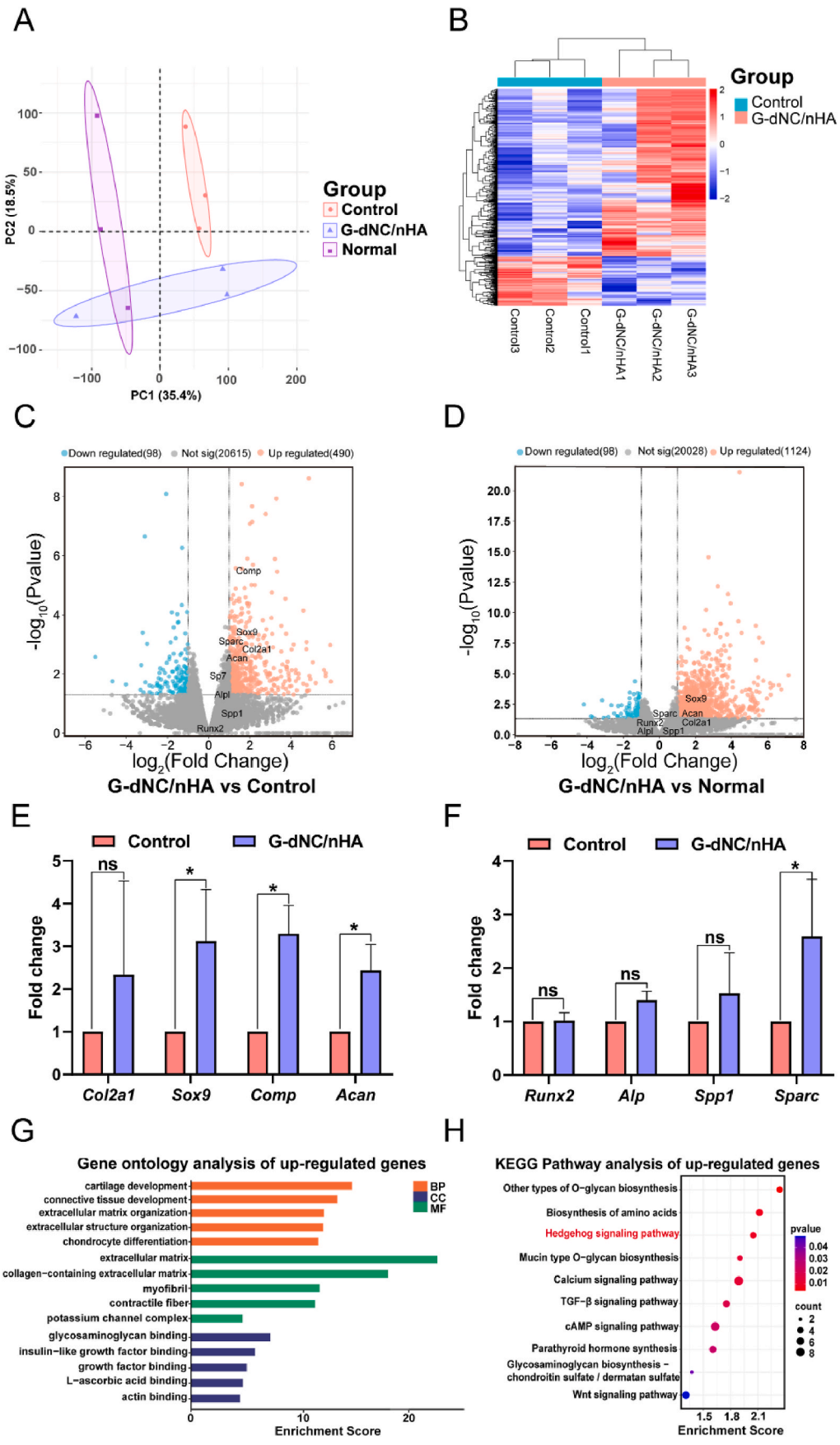

(caption on next page)

Fig. 8. RNA sequencing of the osteochondral regeneration samples at week 12. A) Principal component analysis (PCA) of the osteochondral tissue transcriptome from the Normal, G-dNC/nHA, Control groups. B) heatmap of the differentially expressed genes (DEGs) in the G-dNC/nHA group and the Control group. C, D) Volcano diagram of G-dNC/nHA vs. control (negative control) groups and G-dNC/nHA vs. normal (positive control) groups. E, F) Relative expression levels of chondrogenesis and osteogenesis of G-dNC/nHA and control groups. G) Gene ontology enrichment and H) Kyoto Encyclopedia of Genes and Genomes enrichment analysis of up-regulated genes of the G-dNC/nHA group relative to the control group. All data were analyzed by a *t*-test analysis and error bars indicate Mean ± SD, $^{*}p < 0.05$, $^{**}p < 0.01$, $^{***}p < 0.001$."ns" represents no significance.

control groups and experimental model environments. Gene Ontology (GO) enrichment analysis included biological process (BP), cellular component (CC), and molecular function (MF). The significantly enriched upregulated GO terms, including cartilage development, chondrocyte differentiation, glycosaminoglycans, growth factors, and more, indicate that G-dNC/nHA scaffold could modulate BMSCs and chondrocytes development (Fig. 8G, Figure S17). In addition, the Kyoto Encyclopedia of Genes and Genomes (KEGG) pathway analysis revealed significant upregulation, including the Hedgehog, TGF-β, Wnt, and cAMP signaling pathways (Fig. 8G). The Hedgehog and TGF-β pathways have been widely reported to be associated with the process of cartilage development [45,46], while the Wnt and cAMP signaling pathways are reportedly associated with osteogenesis in the corresponding literature [47,48]. KEGG pathway analysis showed that the Hedgehog signaling pathway was more significant than the other pathways, indicating that the difference between the G-dNC/nHA and control groups was reflected in chondrogenesis. This conclusion was consistent with the results of IHC and volcano plots. Hence, we hypothesized that the G-dNC/nHA scaffold facilitates chondrogenesis via the Hedgehog pathway.

The Hedgehog (Hh) ligand protein in the Hedgehog pathway binds to the receptor Ptch1. Subsequently, the smoothened (Smo) is activated. The Smo activates the Gli protein family of transcription factors, thereby regulating the expression of downstream target genes (Figure S18). To further confirm activation of the G-dNC/nHA scaffold, Gli1 protein expression was detected by IF and Western blotting (WB). WB and IF results showed that the expression of the Gli1 protein in the G-dNC/nHA group was higher than that in the control group (Figure S19 and S20). Thus, the Hedgehog pathway plays a significant role in cartilage development. The IHC results for COL II showed that the tissue in the G-dNC/nHA group changed from a mixed collagen phenotype to a hyaline phenotype from 6 weeks to 12 weeks. The Hedgehog pathway, which promotes cell proliferation and tissue remodeling, may play a critical role in cartilage development. In summary, the G-dNC/nHA scaffold provided a favorable physical and chemical microenvironment for cell development, promoting osteochondral regeneration.

4. Conclusion

Regeneration of osteochondral defects requires a gradient-integrated scaffold with calcification layers to guide hyaline cartilage regeneration. Therefore, a novel class of multi-crosslinked polysaccharide-based 3D printing inks was successfully developed in this study to fabricate an osteochondral integrated scaffold. Innovative printing strategies, including dual-nozzle cross-printing technology and gradient cross-linking, were employed to create gradient bilayer scaffolds featuring a calcification layer. Mechanical assessments confirmed the robust mechanical properties of the scaffold in terms of compressive and shear resistances. The excellent regeneration of osteochondral tissue with hyaline cartilage was attributed to the gradient of bioactive scaffolds with a calcification layer *in vivo*. The bioactive scaffold with dNC and nHA simultaneously stimulated cell behavior to regenerate hyaline cartilage and the subchondral bone. The presence of a calcification layer enhanced the integration of regenerated bone and cartilage. The findings of this study provide the molecular mechanism theory and the experimental groundwork for constructing osteochondral defect transplant substitutes with biomimetic compositions and structures in the future.

CRediT authorship contribution statement

Zhonglian Wu: Writing – original draft, Data curation, Conceptualization. **Hang Yao:** Funding acquisition, Formal analysis. **Haidi Sun:** Formal analysis. **Zehao Gu:** Software. **Xu Hu:** Methodology. **Jian Yang:** Methodology. **Junli Shi:** Data curation. **Haojun Yang:** Data curation. **Jihang Dai:** Investigation. **Hui Chong:** Methodology. **Dong-An Wang:** Methodology. **Liwei Lin:** Writing – review & editing. **Wang Zhang:** Writing – review & editing, Supervision, Resources.

Declaration of competing interest

The authors declare that they have no known competing financial interests or personal relationships that could have appeared to influence the work reported in this paper.

Data availability

Data will be made available on request.

Acknowledgments

This work was supported by Young scientists lifting project of Jiangsu Province, China (TJ-2022-072), Yantai Science and Technology Plan Project (2022MSGY072), and the Natural Science Foundation of Jiangsu Province (BK20190903and BX2023026).

Appendix A. Supplementary data

Supplementary data to this article can be found online at https://doi.org/10.1016/j.mtbio.2024.101080.

References

[1] J. Martel-Pelletier, A.J. Barr, F.M. Cicuttini, P.G. Conaghan, C. Cooper, M. B. Goldring, S.R. Goldring, G. Jones, A.J. Teichtahl, J.-P. Pelletier, Osteoarthritis, Nat. Rev. Dis. Prim. 2 (1) (2016) 16072, https://doi.org/10.1038/nrdp.2016.72.
[2] X. Niu, N. Li, Z. Du, X. Li, Integrated gradient tissue-engineered osteochondral scaffolds: challenges, current efforts and future perspectives, Bioact. Mater. 20 (2023) 574–597, https://doi.org/10.1016/j.bioactmat.2022.06.011.
[3] W. Wei, H. Dai, Articular cartilage and osteochondral tissue engineering techniques: recent advances and challenges, Bioact. Mater. 6 (12) (2021) 4830–4855, https://doi.org/10.1016/j.bioactmat.2021.05.011.
[4] D.J. Huey, J.C. Hu, K.A. Athanasiou, Unlike bone, cartilage regeneration remains elusive, Science 338 (6109) (2012) 917–921, https://doi.org/10.1126/science.1222454.
[5] M.A.J. Finnilä, S. Das Gupta, M.J. Turunen, I. Hellberg, A. Turkiewicz, V. Lutz-Bueno, E. Jonsson, M. Holler, N. Ali, V. Hughes, H. Isaksson, J. Tjörnstrand, P. Önnerfjord, M. Guizar-Sicairos, S. Saarakkala, M. Englund, Mineral crystal thickness in calcified cartilage and subchondral bone in healthy and osteoarthritic human knees, J. Bone Miner. Res. 37 (9) (2022) 1700–1710, https://doi.org/10.1002/jbmr.4642.
[6] S. Barui, D. Ghosh, C.T. Laurencin, Osteochondral regenerative engineering: challenges, state-of-the-art and translational perspectives, Regenerative Biomaterials 10 (2023) rbac109, https://doi.org/10.1093/rb/rbac109.
[7] Z. Wang, H. Le, Y. Wang, H. Liu, Z. Li, X. Yang, C. Wang, J. Ding, X. Chen, Instructive cartilage regeneration modalities with advanced therapeutic implantations under abnormal conditions, Bioact. Mater. 11 (2022) 317–338, https://doi.org/10.1016/j.bioactmat.2021.10.002.
[8] Z. Qiao, M. Lian, Y. Han, B. Sun, X. Zhang, W. Jiang, H. Li, Y. Hao, K. Dai, Bioinspired stratified electrowritten fiber-reinforced hydrogel constructs with layer-specific induction capacity for functional osteochondral regeneration, Biomaterials 266 (2021) 120385, https://doi.org/10.1016/j.biomaterials.2020.120385.
[9] M. Lian, B. Sun, Y. Han, B. Yu, W. Xin, R. Xu, B. Ni, W. Jiang, Y. Hao, X. Zhang, Y. Shen, Z. Qiao, K. Dai, A low-temperature-printed hierarchical porous sponge-like

scaffold that promotes cell-material interaction and modulates paracrine activity of MSCs for vascularized bone regeneration, Biomaterials 274 (2021) 120841, https://doi.org/10.1016/j.biomaterials.2021.120841.
[10] X. Nie, Y.J. Chuah, P. He, D.-A. Wang, Engineering a multiphasic, integrated graft with a biologically developed cartilage–bone interface for osteochondral defect repair, J. Mater. Chem. B 7 (42) (2019) 6515–6525, https://doi.org/10.1039/C9TB00822E.
[11] Y. Gong, K. Su, T.T. Lau, R. Zhou, D.-A. Wang, Microcavitary hydrogel-mediating phase transfer cell culture for cartilage tissue engineering, Tissue Eng. 16 (12) (2010) 3611–3622, https://doi.org/10.1089/ten.tea.2010.0219.
[12] K.S. Allan, R.M. Pilliar, J. Wang, M.D. Grynpas, R.A. Kandel, Formation of biphasic constructs containing cartilage with a calcified zone interface, Tissue Eng. 13 (1) (2007) 167–177, https://doi.org/10.1089/ten.2006.0081.
[13] J. Xing, X. Peng, A. Li, M. Chen, Y. Ding, X. Xu, P. Yu, J. Xie, J. Li, Gellan gum/alginate-based Ca-enriched acellular bilayer hydrogel with robust interface bonding for effective osteochondral repair, Carbohydrate Polymers 270 (2021) 118382, https://doi.org/10.1016/j.carbpol.2021.118382.
[14] H. Da, S.-J. Jia, G.-L. Meng, J.-H. Cheng, W. Zhou, Z. Xiong, Y.-J. Mu, J. Liu, The impact of compact layer in biphasic scaffold on osteochondral tissue engineering, PLoS One 8 (1) (2013) e54838, https://doi.org/10.1371/journal.pone.0054838.
[15] T.J. Levingstone, A. Matsiko, G.R. Dickson, F.J. O'Brien, J.P. Gleeson, A biomimetic multi-layered collagen-based scaffold for osteochondral repair, Acta Biomater. 10 (5) (2014) 1996–2004, https://doi.org/10.1016/j.actbio.2014.01.005.
[16] J. Gao, X. Ding, X. Yu, X. Chen, X. Zhang, S. Cui, J. Shi, J. Chen, L. Yu, S. Chen, J. Ding, Cell-free bilayered porous scaffolds for osteochondral regeneration fabricated by continuous 3D-printing using nascent physical hydrogel as ink, Adv. Healthcare Mater. 10 (3) (2021) 2001404, https://doi.org/10.1002/adhm.202001404.
[17] X. Liu, Y. Wei, C. Xuan, L. Liu, C. Lai, M. Chai, Z. Zhang, L. Wang, X. Shi, A biomimetic biphasic osteochondral scaffold with layer-specific release of stem cell differentiation inducers for the reconstruction of osteochondral defects, Adv. Healthcare Mater. 9 (23) (2020) 2000076, https://doi.org/10.1002/adhm.202000076.
[18] R.M. Jeuken, A.K. Roth, R.J.R.W. Peters, C.C. Van Donkelaar, J.C. Thies, L.W. Van Rhijn, P.J. Emans, Polymers in cartilage defect repair of the knee: current status and future prospects, Polymers (2016).
[19] Y.-J. Kim, R.L.Y. Sah, J.-Y.H. Doong, A.J. Grodzinsky, Fluorometric assay of DNA in cartilage explants using Hoechst 33258, Anal. Biochem. 174 (1) (1988) 168–176, https://doi.org/10.1016/0003-2697(88)90532-5.
[20] J.E. Stone, N. Akhtar, S. Botchway, C.A. Pennock, Interaction of 1,9-dimethyl-methylene blue with glycosaminoglycans, Ann. Clin. Biochem. 31 (2) (1994) 147–152, https://doi.org/10.1177/000456329403100206.
[21] D.D. Cissell, J.M. Link, J.C. Hu, K.A. Athanasiou, A modified hydroxyproline assay based on hydrochloric acid in ehrlich's solution accurately measures tissue collagen content, Tissue Eng. C Methods 23 (4) (2017) 243–250, https://doi.org/10.1089/ten.tec.2017.0018.
[22] P. Chen, J. Tao, S. Zhu, Y. Cai, Q. Mao, D. Yu, J. Dai, H. Ouyang, Radially oriented collagen scaffold with SDF-1 promotes osteochondral repair by facilitating cell homing, Biomaterials 39 (2015) 114–123, https://doi.org/10.1016/j.biomaterials.2014.10.049.
[23] B. Zhang, X. Pei, P. Song, H. Sun, H. Li, Y. Fan, Q. Jiang, C. Zhou, X. Zhang, Porous bioceramics produced by inkjet 3D printing: effect of printing ink formulation on the ceramic macro and micro porous architectures control, Compos. B Eng. 155 (2018) 112–121, https://doi.org/10.1016/j.compositesb.2018.08.047.
[24] G.S. Hussey, J.L. Dziki, S.F. Badylak, Extracellular matrix-based materials for regenerative medicine, Nat. Rev. Mater. 3 (7) (2018) 159–173, https://doi.org/10.1038/s41578-018-0023-x.
[25] F. Pati, J. Jang, D.-H. Ha, S. Won Kim, J.-W. Rhie, J.-H. Shim, D.-H. Kim, D.-W. Cho, Printing three-dimensional tissue analogues with decellularized extracellular matrix bioink, Nat. Commun. 5 (1) (2014) 3935, https://doi.org/10.1038/ncomms4935.
[26] K.S. Lim, B.S. Schon, N.V. Mekhileri, G.C.J. Brown, C.M. Chia, S. Prabakar, G. J. Hooper, T.B.F. Woodfield, New visible-light photoinitiating system for improved print fidelity in gelatin-based bioinks, ACS Biomater. Sci. Eng. 2 (10) (2016) 1752–1762, https://doi.org/10.1021/acsbiomaterials.6b00149.
[27] A. Schwab, R. Levato, M. D'Este, S. Piluso, D. Eglin, J. Malda, Printability and shape fidelity of bioinks in 3D bioprinting, Chem. Rev. 120 (19) (2020) 11028–11055, https://doi.org/10.1021/acs.chemrev.0c00084.
[28] Z. Zheng, M. Zhang, Z. Liu, Investigation on evaluating the printable height and dimensional stability of food extrusion-based 3D printed foods, J. Food Eng. 306 (2021) 110636, https://doi.org/10.1016/j.jfoodeng.2021.110636.
[29] S. Shin, J. Hyun, Rheological properties of cellulose nanofiber hydrogel for high-fidelity 3D printing, Carbohydrate Polymers 263 (2021) 117976, https://doi.org/10.1016/j.carbpol.2021.117976.
[30] H. Zhang, H. Huang, G. Hao, Y. Zhang, H. Ding, Z. Fan, L. Sun, 3D printing hydrogel scaffolds with nanohydroxyapatite gradient to effectively repair osteochondral defects in rats, Adv. Funct. Mater. 31 (1) (2021) 2006697, https://doi.org/10.1002/adfm.202006697.
[31] B. You, Q. Li, H. Dong, T. Huang, X. Cao, H. Liao, Bilayered HA/CS/PEGDA hydrogel with good biocompatibility and self-healing property for potential application in osteochondral defect repair, J. Mater. Sci. Technol. 34 (6) (2018) 1016–1025, https://doi.org/10.1016/j.jmst.2017.11.016.
[32] P. Xu, H. Xu, Y. Yang, X. Wang, W. An, Y. Hu, S. Xu, A nonswellable gradient hydrogel with tunable mechanical properties, J. Mater. Chem. B 8 (13) (2020) 2702–2708, https://doi.org/10.1039/D0TB00296H.
[33] D. Gan, Z. Wang, C. Xie, X. Wang, W. Xing, X. Ge, H. Yuan, K. Wang, H. Tan, X. Lu, Mussel-inspired tough hydrogel with in situ nanohydroxyapatite mineralization for osteochondral defect repair, Adv. Healthcare Mater. 12 (2) (2023) 2203040, https://doi.org/10.1002/adhm.202203040.
[34] S.S. Shah, H. Liang, S. Pandit, Z. Parikh, J.A. Schwartz, T. Goldstein, L.P. Lavelle, A. Datta, D.A. Grande, Optimization of degradation profile for new scaffold in cartilage repair, CARTILAGE 9 (4) (2017) 438–449, https://doi.org/10.1177/1947603517700954.
[35] T. Chen, J. Bai, J. Tian, P. Huang, H. Zheng, J. Wang, A single integrated osteochondral in situ composite scaffold with a multi-layered functional structure, Colloids Surf. B Biointerfaces 167 (2018) 354–363, https://doi.org/10.1016/j.colsurfb.2018.04.029.
[36] J. Lee, S.J. Oh, S.H. An, W.-D. Kim, S.-H. Kim, Machine learning-based design strategy for 3D printable bioink: elastic modulus and yield stress determine printability, Biofabrication 12 (3) (2020) 035018, https://doi.org/10.1088/1758-5090/ab8707.
[37] D.A. Cantu, W.J. Kao, Combinatorial biomatrix/cell-based therapies for restoration of host tissue architecture and function, Adv. Healthcare Mater. 2 (12) (2013) 1544–1563, https://doi.org/10.1002/adhm.201300063.
[38] M. Farokhi, F. Jonidi Shariatzadeh, A. Solouk, H. Mirzadeh, Alginate based scaffolds for cartilage tissue engineering: a review, International Journal of Polymeric Materials and Polymeric Biomaterials 69 (4) (2020) 230–247, https://doi.org/10.1080/00914037.2018.1562924.
[39] L. Ouyang, C.B. Highley, W. Sun, J.A. Burdick, A generalizable strategy for the 3D bioprinting of hydrogels from nonviscous photo-crosslinkable inks, Adv. Mater. 29 (8) (2017) 1604983, https://doi.org/10.1002/adma.201604983.
[40] X. Yang, Z. Lu, H. Wu, W. Li, L. Zheng, J. Zhao, Collagen-alginate as bioink for three-dimensional (3D) cell printing based cartilage tissue engineering, Mater. Sci. Eng. C 83 (2018) 195–201, https://doi.org/10.1016/j.msec.2017.09.002.
[41] C. Gentili, R. Cancedda, Cartilage and bone extracellular matrix, Curr. Pharmaceut. Des. 15 (12) (2009) 1334–1348, https://doi.org/10.2174/138161209787846739.
[42] W. Dai, L. Zhang, Y. Yu, W. Yan, F. Zhao, Y. Fan, C. Cao, Q. Cai, X. Hu, Y. Ao, 3D bioprinting of heterogeneous constructs providing tissue-specific microenvironment based on host–guest modulated dynamic hydrogel bioink for osteochondral regeneration, Adv. Funct. Mater. 32 (23) (2022) 2200710, https://doi.org/10.1002/adfm.202200710.
[43] X. Nie, J. Yang, Y.J. Chuah, W. Zhu, Y. Peck, P. He, D.-A. Wang, Full-scale osteochondral regeneration by sole graft of tissue-engineered hyaline cartilage without Co-engraftment of subchondral bone substitute, Adv. Healthcare Mater. 9 (2) (2020) 1901304, https://doi.org/10.1002/adhm.201901304.
[44] H. Park, H.J. Lee, H. An, K.Y. Lee, Alginate hydrogels modified with low molecular weight hyaluronate for cartilage regeneration, Carbohydrate Polymers 162 (2017) 100–107, https://doi.org/10.1016/j.carbpol.2017.01.045.
[45] Z. Yang, B. Wang, W. Liu, X. Li, K. Liang, Z. Fan, J.J. Li, Y. Niu, Z. He, H. Li, D. Wang, J. Lin, Y. Du, J. Lin, D. Xing, In situ self-assembled organoid for osteochondral tissue regeneration with dual functional units, Bioact. Mater. 27 (2023) 200–215, https://doi.org/10.1016/j.bioactmat.2023.04.002.
[46] T. Xu, Y. Yang, E.H.-L. Yeung, Q. Chen, H.-P. Bei, Q. Yang, M. Yang, Y. Hao, B. Li, X. Zhao, Injectable, self-contained, subaqueously cross-linking laminous adhesives for biophysical-chemical modulation of osteochondral microenvironment, Adv. Funct. Mater. 33 (23) (2023) 2213428, https://doi.org/10.1002/adfm.202213428.
[47] B. Yuan, Y. Zhang, R. Zhao, H. Lin, X. Yang, X. Zhu, K. Zhang, A.G. Mikos, X. Zhang, A unique biomimetic modification endows polyetherketoneketone scaffold with osteoinductivity by activating cAMP/PKA signaling pathway, Sci. Adv. 8(40) eabq7116. https://doi.org/10.1126/sciadv.abq7116..
[48] T. Wang, W. Xu, X. Zhao, B. Bai, Y. Hua, J. Tang, F. Chen, Y. Liu, Y. Wang, G. Zhou, Y. Cao, Repair of osteochondral defects mediated by double-layer scaffolds with natural osteochondral-biomimetic microenvironment and interface, Materials Today Bio 14 (2022) 100234, https://doi.org/10.1016/j.mtbio.2022.100234.